Vietnam Journal of Catalysis and Adsorption
Tạp chí xúc tác và hấp phụ Việt Nam

http://jca.edu.vn

Synthesis of Nanocarbon from Waste Engine Oil via Solution Plasma Process for Lithium-Ion Battery Anodes

Nguyen Van Thai[2], Ngo Ha Son[3], Le Huu Thanh[1], Pham Trung Kien[1], Vu Tri Thien[1,*]

[1] *Institute of Materials, Biology and Environment, Academy of Military Science and Technology*
[2] *Institute Weapon, 51 Phu Dien street, Hanoi, VIETNAM*
[3] *Hanoi University of Mining and Geology, 18 Vien street, Hanoi*
** Email: Thienkqh140309@gmail.com*

ARTICLE INFO

Received: 07/05/2026
Accepted: 21/05/2026
Published: 30/06/2026

Keywords:
waste engine oil;
solution plasma;
nanocarbon;
lithium-ion batteries

ABSTRACT

With the increasing demand for sustainable energy storage materials, the conversion of waste engine oil into functional carbon materials has attracted considerable attention due to its dual benefits of environmental remediation and value-added material production. In this study, nanocarbon materials were directly synthesized from waste engine oil via a solution plasma process under room temperature and atmospheric pressure conditions. The as-synthesized materials were systematically characterized using SEM-EDS, TEM, Raman spectroscopy, and X-ray diffraction (XRD), while their electrochemical properties were evaluated by cyclic voltammetry (CV), galvanostatic charge–discharge (GCD), and electrochemical impedance spectroscopy (EIS). The results revealed that the obtained nanocarbon partially graphitized outer layers surrounding amorphous carbon domains with particle sizes ranging from approximately 20 to 50 nm. The material exhibited typical electrochemical behavior of carbonaceous anodes for lithium-ion batteries, delivering a specific capacity of approximately 250 $mAh.g^{-1}$ at a current density of 100 $mA.g^{-1}$ and maintaining stable cycling performance over 200 charge-discharge cycles.

Introduction

The rapid development of renewable energy technologies, such as solar energy, wind power, and electrochemical energy systems, has significantly increased the demand for high-performance energy storage devices [1–4]. Among them, lithium-ion batteries (LIBs) have become one of the most important energy storage technologies owing to their high energy density, long cycle life, and wide applicability in portable electronics, electric vehicles, and large-scale energy storage systems. The electrochemical performance of LIBs strongly depends on the structural and chemical properties of electrode materials [5], [6]. In recent years, carbon-based materials, including graphite, graphene, amorphous carbon, and carbon nanotubes, have been extensively investigated due to their excellent electrical conductivity, high chemical stability, and effective lithium-ion storage capability [7–10]. However, most commercial carbon materials are still derived from non-renewable fossil-based precursors and typically require high-temperature, energy-intensive synthesis processes. Alongside the growing demand for

https://doi.org/10.62239/jca.2026.023
46

advanced electrode materials, the treatment of waste engine oil has also emerged as a serious environmental concern. Waste engine oil contains large amounts of long-chain hydrocarbons, polycyclic aromatic compounds, and heavy-metal-containing additives, which can cause severe soil and water contamination if improperly disposed of [11, 12]. Nevertheless, owing to its high carbon content and homogeneous liquid nature, waste engine oil is considered a promising carbon precursor for the synthesis of value-added carbon materials [13], [14].

Recently, the solution plasma process (SPP) has attracted considerable attention as an efficient approach for the direct synthesis of carbon nanomaterials in liquid media [15, 16]. Compared with conventional thermal methods, SPP enables the formation of carbon materials at room temperature and atmospheric pressure without the need for vacuum systems or metal catalysts [17]. In the plasma environment, high-energy electrons and reactive species are generated, which can rapidly decompose complex hydrocarbon chains, thereby promoting carbonization and the formation of defect-rich nanocarbon structures with high specific surface area [18–21]. Despite the increasing interest in waste-derived carbon materials for lithium-ion battery applications, the direct conversion of hazardous waste engine oil into electrochemically active nanocarbon materials via low-temperature solution plasma remains rarely reported. In particular, the synthesis of semi-graphitic nanocarbon from waste engine oil under mild plasma conditions for use as LIB anode materials has not been sufficiently investigated. Therefore, this study aims to develop a simple and sustainable plasma-assisted route for converting waste engine oil into value-added nanocarbon materials and to evaluate their electrochemical performance as anode materials for lithium-ion batteries.

This study focuses on the synthesis of nanocarbon materials from waste engine oil via a solution plasma process and evaluates their potential application as anode materials for lithium-ion batteries.

Experimental

Materials

Waste engine oil was collected from local automotive repair shops and filtered to remove suspended impurities and solid residues prior to use. Benzene (99.5%, Xilong, China), ethanol (C_2H_5OH, 99.7%, Gelon, China), and tungsten electrodes (99.9% purity, China) were used in the experiments.

A high-voltage power supply system manufactured by PEKURIS (Japan) was employed to generate the solution plasma. The discharge characteristics were monitored using a Siglent SDS1104CFL digital oscilloscope (100 MHz, 4 channels).

Fabrication of materials

Synthesis nanocarbon

The filtered waste engine oil was mixed with benzene at a volume ratio of 80:20. A pair of tungsten electrodes with a diameter of 3 mm was employed, and the interelectrode gap was fixed at 1 mm. The electrodes were insulated using high-temperature-resistant Teflon tubes. A pulsed voltage of 2 kV with a frequency of 20 kHz and a pulse width of 1 µs was applied to generate the plasma discharge. The plasma process was continuously maintained for 60 min under vigorous magnetic stirring and water-cooling conditions. After the reaction, the obtained product was filtered and repeatedly washed with benzene and ethanol to remove residual organic species, followed by drying to obtain the carbon material. A schematic illustration of the synthesis process is presented in Fig. 1a.

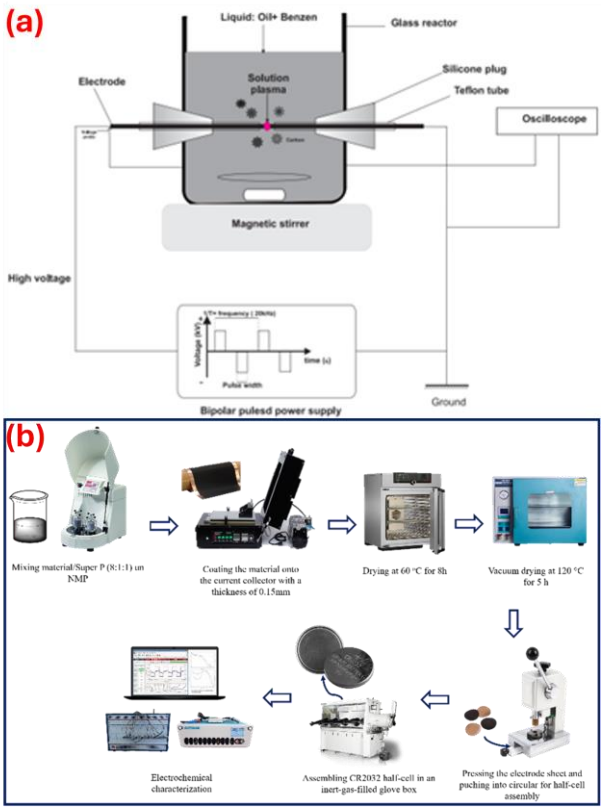

Fig 1: Schematic illustration of the synthesis process of carbon materials from waste engine oil (a); Schematic illustration of the electrode fabrication process (b).

Electrode Fabrication

Prior to electrochemical evaluation, the as-prepared carbon material was mixed with other components to fabricate the electrode. The slurry was prepared by mixing the carbon material, PVDF binder, and Super P conductive carbon in a weight ratio of 8:1:1 using an appropriate amount of N-methyl-2-pyrrolidone (NMP) solvent in a ball mill until a homogeneous viscous mixture was obtained. The resulting slurry was then coated onto carbon-coated copper foil using a doctor blade technique and dried under vacuum at 80 °C for 24 h to obtain the electrode sheet. The dried electrode sheet was punched into circular electrodes with a diameter of 10 mm. Each electrode was weighed using an analytical balance to determine the actual mass loading of the active material, which was controlled within the range of 1÷2 mg cm^{-2} for the calculation of current density and specific capacity during electrochemical measurements. The prepared electrodes were subsequently assembled into CR2032 coin cells. A schematic summary of the experimental procedure is illustrated in Fig 1b.

Research methods

The morphology and chemical composition of the synthesized materials were characterized by scanning electron microscopy coupled with energy-dispersive X-ray spectroscopy (SEM-EDS) using a HITACHI S-4800 instrument, and transmission electron microscopy (TEM) using a JEOL JEM-1010 microscope at the Institute of Materials Science, Vietnam Academy of Science and Technology. The phase composition and crystal structure of the materials were analyzed by X-ray diffraction (XRD) using a MiniFlex 600 Rigaku diffractometer (Japan) at the VNU University of Science, Vietnam National University, Hanoi. The measurements were carried out using CuKα radiation with a wavelength of λ = 1.5406 A° over a 2θ range of 20–70° at a scanning rate of 0.03 °/s. Raman spectra were recorded with a 532 nm laser source (Renishaw inVia). X-ray photoelectron spectroscopy (XPS, Thermo Scientific ESCALAB 250Xi) was employed to determine surface valence states.

Electrochemical properties were evaluated by cyclic voltammetry (CV) at a scan rate of 0.1 mV/s and galvanostatic charge-discharge (GCD) measurements at a current density of 100 mA/g using a WonATech-WBCS 3000L32 electrochemical workstation (Korea). Electrochemical impedance spectroscopy (EIS) measurements were performed using an AUTOLAB electrochemical analyzer (Switzerland).

Results and discussion

Morphological and Structural Characterization

The morphology of the synthesized nanocarbon was investigated by SEM (Fig 2a, b) and TEM (Fig 2c, d). The results indicate that the material possesses a relatively uniform nanostructure and mainly consists of carbon nanoparticles aggregated into a three-dimensional interconnected network. In the low-magnification SEM image (Fig 2a), the material appears as uniformly distributed agglomerated particle clusters over the entire surface. These nanoparticles tend to aggregate and interconnect, forming a continuous porous structure. Such aggregation behavior is commonly observed in nanocarbon materials synthesized by solution plasma due to the high surface energy of the newly formed nanoparticles. The higher-magnification SEM image (Fig 2b) further reveals a quasi-spherical morphology, with particle sizes estimated to be in the range of several tens of nanometers.

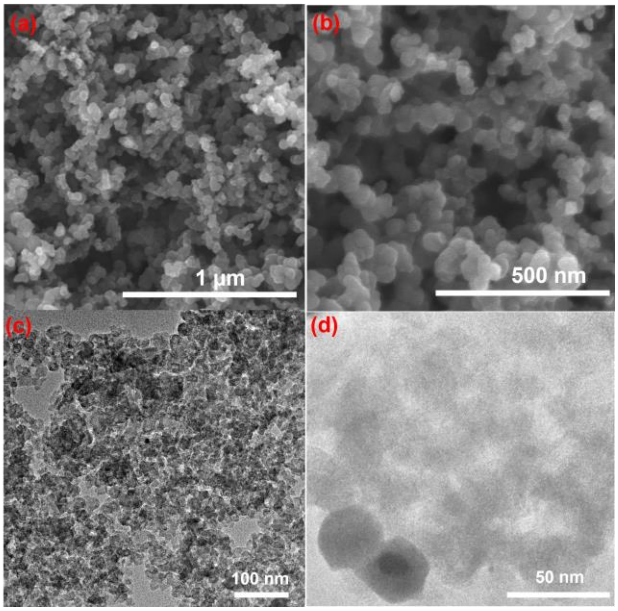

Fig 2: SEM images (a,b) and TEM images (c,d) of the carbon material.

The low-resolution TEM image (Fig 2c) confirms that the material is composed of densely distributed carbon nanoparticles aggregated into a continuous network. The relatively blurred particle boundaries suggest a low degree of crystallinity, indicating that the material mainly exists in a semi-amorphous or poorly ordered graphitic state. The high-resolution TEM image (Fig 2d) clearly shows quasi-spherical carbon nanoparticles with sizes ranging from approximately 20 to 50 nm. Some particles exhibit a darker contrast in the core region and a brighter outer region, indicating the possible formation of a core–shell structure. The outer shell

https://doi.org/10.62239/jca.2026.023

appears relatively thin and uniform, which may originate from graphitic carbon layers surrounding an amorphous carbon core during the plasma-assisted synthesis process.

The Raman spectra and XRD patterns of the synthesized nanocarbon are presented in Fig 3. The Raman spectrum (Fig 3a) exhibits characteristic D (~1350 cm^{-1}), G (~1580 cm^{-1}), and 2D (~2700 cm^{-1}) bands, indicating the formation of semi-graphitic carbon structures. The D band is associated with structural defects and amorphous carbon regions, whereas the G band corresponds to the in-plane vibration of sp^2 bonded carbon atoms in graphitic domains [22].

In addition, the XRD pattern (Fig 3b) shows two broad diffraction peaks located at approximately $2\theta \approx 26^{o}$ and 43^{o}, corresponding to the (002) and (100) crystal planes of graphitic carbon, respectively. The broad nature of these diffraction peaks suggests that the material predominantly exists in a semi-amorphous state with an incomplete degree of graphitization. The Raman and XRD results are in good agreement, confirming that the obtained material consists of defect-rich semi-graphitic nanocarbon structures. Such structural characteristics are considered favorable for lithium-ion battery anode applications, as they provide both good electrical conductivity and additional active sites for Li^+ storage [23].

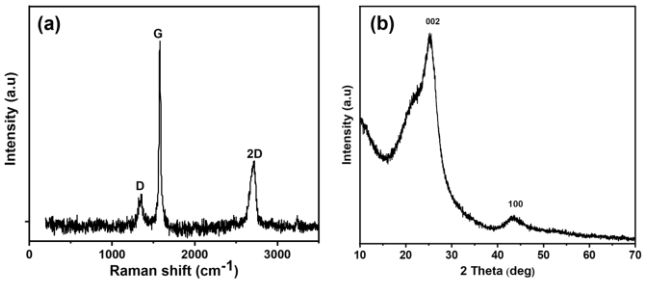

Fig 3: Raman spectrum (a) and X-ray diffraction pattern (b) of the nanocarbon material.

The EDX spectrum and elemental mapping results of the synthesized nanocarbon are presented in Fig 4. The EDX spectrum (Fig 4a) reveals that the material mainly consists of carbon and oxygen elements. The carbon peak exhibits a significantly higher intensity, indicating that carbon is the dominant component of the synthesized material. In contrast, the oxygen signal is considerably weaker, suggesting a relatively low oxygen content. Moreover, no distinct peaks corresponding to metallic elements or other impurities were detected, implying that the obtained nanocarbon possesses relatively high purity.

The EDX elemental mapping results further demonstrate that carbon (Fig 4b) is continuously and uniformly distributed throughout the entire surface of the nanocarbon aggregates. Meanwhile, oxygen (Fig 4c) is also distributed across the investigated area but with a much lower density. The homogeneous distribution of oxygen suggests the presence of oxygen-containing functional groups on the surface of the nanocarbon, which may originate from the solution plasma process or surface oxidation after synthesis. These oxygen-containing groups are expected to improve the wettability of the electrode toward the electrolyte and facilitate Li^+ ion diffusion during electrochemical operation.

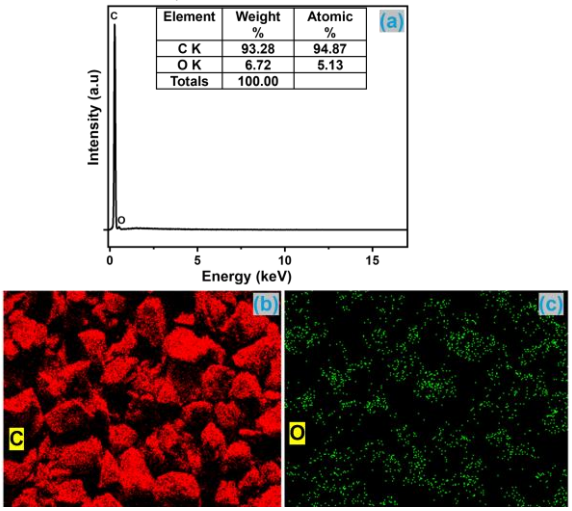

Fig 4: EDX spectrum (a) and EDX elemental mapping images of carbon (b) and oxygen (c) in the nanocarbon material.

Electrochemical performance

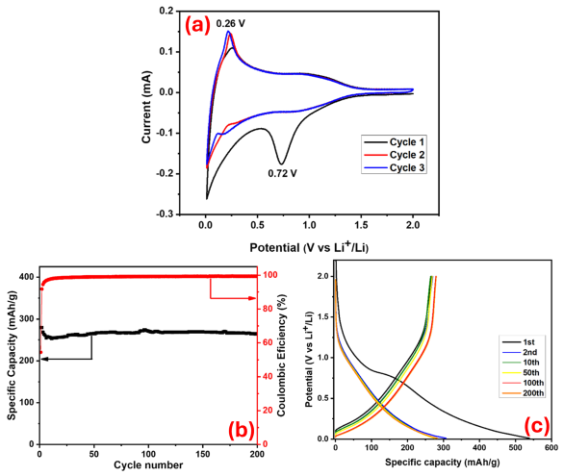

Fig 5: Cyclic voltammetry (CV) curves of the nanocarbon material for the first three cycles at a scan rate of 0.1 mV/s within the potential range of 0÷2 V (a); Coulombic efficiency and specific capacity (b), and charge–discharge profiles of the nanocarbon material at different cycles under a current density of 100 mA.g-1 within the potential range of 0÷2 V (c)

https://doi.org/10.62239/jca.2026.023

The cyclic voltammetry (CV) curves of the nanocarbon electrode during the first three cycles are presented in Fig 5a. The results indicate that the material exhibits typical electrochemical characteristics of carbonaceous anodes for lithium-ion batteries. During the first cathodic scan, a pronounced reduction peak appears in the potential range of approximately 0.6÷0.8 V, which is associated with electrolyte decomposition and the formation of the solid electrolyte interphase (SEI) layer on the electrode surface. The intensity of this peak decreases significantly in the subsequent cycles, indicating that the SEI layer becomes gradually stabilized after the initial cycle.

In the low-potential region, the CV curves exhibit characteristic redox peaks corresponding to the insertion/extraction of Li^+ ions within the nanocarbon structure. From the second to the third cycle, the CV profiles nearly overlap with each other, suggesting good reversibility of the electrochemical reactions as well as high structural stability of the material during the charge-discharge process [24], [25].

The galvanostatic charge-discharge performance of the nanocarbon material is presented in Fig 5b, c. As shown in Fig 5b, the electrode delivers an initial specific capacity of approximately 260÷270 $mAh.g^{-1}$ during the early cycles, followed by a slight decrease and stabilization at around 240÷250 $mAh.g^{-1}$ after 200 charge–discharge cycles. The initial capacity fading can be attributed to the formation of the SEI layer and irreversible side reactions between the electrolyte and the electrode surface during the first cycle. However, after the initial activation process, the specific capacity remains relatively stable with only minor degradation, indicating good cycling stability and effective retention of Li^+ storage sites within the nanocarbon structure. The Coulombic efficiency rapidly increases from approximately 55÷60 % in the first cycle to above 95 % after several cycles and subsequently remains nearly constant at around 99÷100 % throughout the following cycles. This behavior suggests highly reversible Li^+ insertion/extraction processes and the formation of a relatively stable SEI layer on the electrode surface. In addition, the charge–discharge profiles shown in Fig.5c almost overlap from the 10^{th} to the 200^{th} cycle, further demonstrating the excellent electrochemical stability of the nanocarbon electrode during prolonged cycling.

The rate performance of the nanocarbon electrode is presented in Fig 6a. As the current density gradually increases, the specific capacity correspondingly decreases due to enhanced electrochemical polarization and kinetic limitations associated with Li^+ ion diffusion within the electrode structure. At a low current density of 100 $mA.g^{-1}$, the electrode delivers a specific discharge capacity of approximately 250÷260 $mAh.g^{-1}$.

When the current density is increased from 200 mA/g to 4000 mA/g, the specific capacity gradually decreases to approximately 210÷220 $mAh.g^{-1}$, 170÷180 $mAh.g^{-1}$, 130÷140 $mAh.g^{-1}$, and finally 80÷90 $mAh.g^{-1}$ at the highest current density. Despite the decrease in capacity at higher charge–discharge rates, the electrode maintains relatively stable capacities at each current density, indicating that the nanocarbon structure possesses good adaptability under high-rate operating conditions. Notably, when the current density is returned to the initial value, the specific capacity recovers almost completely to approximately 240÷250 $mAh.g^{-1}$. This result demonstrates that the nanocarbon structure remains intact during high-rate cycling and exhibits excellent electrochemical stability.

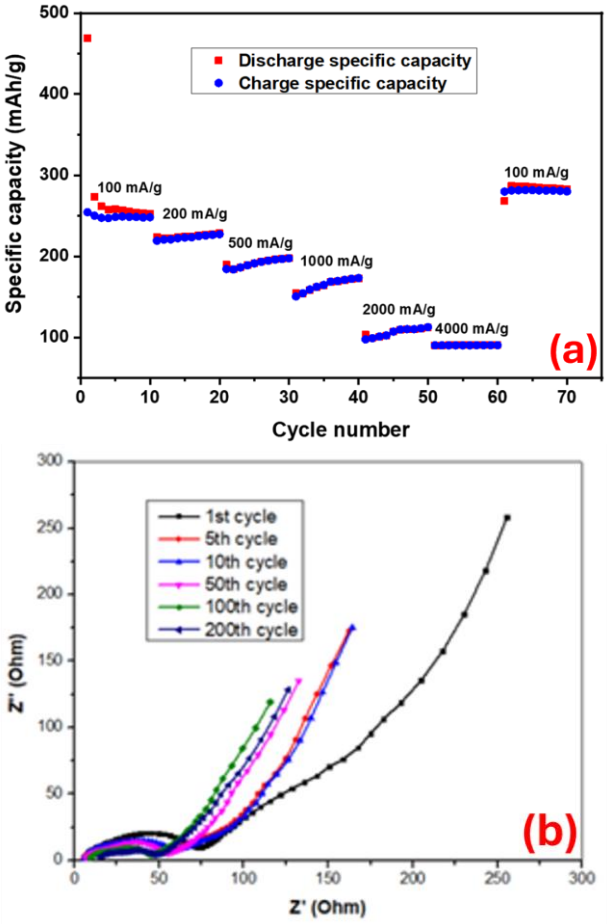

Fig 6: Rate performance of the nanocarbon material at different current densities within the potential range of 0÷2 V (a); Nyquist plots of electrochemical impedance spectroscopy (EIS) of the nanocarbon material at different charge–discharge cycles (b)

https://doi.org/10.62239/jca.2026.023

The electrochemical impedance spectroscopy (EIS) results of the nanocarbon electrode at different charge–discharge cycles are presented in Fig 6b in the form of Nyquist plots. The EIS spectra consist of a semicircle in the high to medium-frequency region and an inclined straight line in the low-frequency region. The semicircle is associated with the charge-transfer resistance (Rct) and the resistance of the SEI layer formed on the electrode surface, whereas the inclined line in the low-frequency region corresponds to Li^+ ion diffusion within the electrode, commonly referred to as Warburg impedance. During the first cycle, the Nyquist plot exhibits the largest semicircle diameter, indicating relatively high charge-transfer resistance. This behavior can be attributed to the initial formation of the SEI layer and the incomplete penetration of the electrolyte into the porous nanocarbon structure. In the subsequent cycles, the semicircle diameter decreases significantly, particularly from the 5^{th} to the 50^{th} cycle, suggesting gradual electrode activation and improved charge-transfer kinetics. The reduction in resistance may result from enhanced electrolyte infiltration into the electrode structure and the progressive stabilization of the SEI layer during cycling.

Table 1. Comparison of waste-derived carbon anode materials for LIBs

Carbon precursor	Synthesis method	Specific capacity	Cycling performance	Ref.
Plane tree leaves	KOH activation carbonization under N_2	460.4 $mAh.g^{-1}$ at 50 $mA.g^{-1}$	Maintained 242 $mAh.g^{-1}$ at 2000 $mA.g^{-1}$	[26]
Lignin-derived carbon	Carbonization /porous carbon preparation	420 $mAh.g^{-1}$	99% retention after 300 cycles at 0.2 $A.g^{-1}$	[27]
Waste tire pyrolysis oil-derived Si/C	CVD-derived S,N-codoped Si/C composite	695 $mAh.g^{-1}$ at 0.05 $A.g^{-1}$	94.6% retention after 500 cycles	[28]
Waste engine oil	Solution plasma process	~250 mAh g^{-1} at 100 mA g^{-1}	Stable over 200 cycles	This work

In addition, the slope of the straight line in the low-frequency region increases with increasing cycle number, indicating improved Li^+ ion diffusion within the electrode. After 100 and 200 cycles, the Nyquist plots remain nearly unchanged without any significant increase in impedance, demonstrating the excellent electrochemical stability of the nanocarbon material during long-term cycling operation.

To further evaluate the electrochemical performance of the synthesized nanocarbon, a comparison with previously reported waste-derived carbon materials for LIB anodes is presented in Table 1. Although the specific capacity is lower than some highly graphitized carbons, the plasma-derived nanocarbon exhibits good cycling stability under mild synthesis conditions without requiring high-temperature treatment or metal catalysts.

Conclusion

Nanocarbon materials were successfully synthesized from waste engine oil via a solution plasma process under room temperature and atmospheric pressure conditions. SEM and TEM analyses revealed aggregated nanocarbon particles with sizes ranging from 20 to 50 nm, forming a porous structure with high surface area. Raman and XRD results confirmed the formation of defect-rich semi-graphitic carbon structures containing both graphitic and amorphous carbon domains. EDX mapping demonstrated that the synthesized material mainly consisted of carbon with a small amount of uniformly distributed oxygen on the surface. Electrochemical measurements indicated that the nanocarbon exhibited typical characteristics of carbonaceous anodes for lithium-ion batteries. The electrode delivered a specific capacity of approximately 250 $mAh.g^{-1}$ at low current density and maintained stable cycling performance over 200 charge-discharge cycles with a Coulombic efficiency close to 100 %. The material also exhibited good rate capability and excellent capacity recovery after cycling at high current densities. In addition, EIS analysis revealed a gradual decrease in charge-transfer resistance during cycling, indicating improved Li^+ ion transport and electrochemical kinetics. These results demonstrate the potential of solution plasma-derived nanocarbon from waste engine oil as an anode material for lithium-ion battery applications.

Acknowledgments

This research is funded by project under contract numbered 04/2025/HĐKHCN-VLSH.

References

1. E. Fan, L. Li, Z. Wang, J. Lin, Y. Huang, Y. Yao, R. Chen, F. Wu, Chem. Rev., 120 (2020) 7020–7063. https://doi.org/10.1021/acs.chemrev.9b00535
2. C. Yan, X. Jiang, J. Yu, Z. Ding, L. Ma, T. Su, Y. Wang, C. Wang, G. Huang, S. Xu, Green Chem., 25 (2023) 3816–3846. https://doi.org/10.1039/D3GC00323J
3. K. Itani, A. De Bernardinis, Energies, 16 (2023) 7530. https://doi.org/10.3390/en16227530
4. N.A.A. Qasem, G.A.Q. Abdulrahman, Int. J. Energy Res., 2024 (2024) 7271748. https://doi.org/10.1155/2024/7271748
5. N. Geetha, D. Kavitha, D. Kumaresan, J. Electrochem. Energy Convers. Storage, 20 (2023) 011013. https://doi.org/10.1115/1.4054735
6. M.Á. Muñoz-Márquez, M. Zarrabeitia, S. Passerini, T. Rojo, Adv. Mater. Interfaces, 9 (2022) 2101773. https://doi.org/10.1002/admi.202101773
7. D.R. Lobato-Peralta, P.U. Okoye, C. Alegre, J. Power Sources, 617 (2024) 235140. https://doi.org/10.1016/j.jpowsour.2024.235140
8. H.S. Gujral, G. Singh, A.V. Baskar, X. Guan, X. Geng, A.V. Kotkondawar, S. Rayalu, P. Kumar, A. Karakoti, A. Vinu, Sci. Technol. Adv. Mater., 23 (2022) 76–119. https://doi.org/10.1080/14686996.2022.2029686
9. L. Li, D. Zhang, J. Deng, Y. Gou, J. Fang, H. Cui, Y. Zhao, M. Cao, Carbon, 183 (2021) 721–734. https://doi.org/10.1016/j.carbon.2021.07.053
10. X. Jiang, Y. Chen, X. Meng, W. Cao, C. Liu, Q. Huang, N. Naik, V. Murugadoss, M. Huang, Z. Guo, Carbon, 191 (2022) 448–470. https://doi.org/10.1016/j.carbon.2022.02.011
11. I.C. Ossai, F.S. Hamid, S.C. Aboudi-Mana, A. Hassan, Environ. Geochem. Health, 46 (2024) 416. https://doi.org/10.1007/s10653-024-02198-7
12. D.M. Armioni, S.A. Raţiu, M.L. Benea, V. Puţan, J. Phys. Conf. Ser., 2927 (2024) 012007. https://doi.org/10.1088/1742-6596/2927/1/012007
13. K.K., B.M.V., N.P., Diam. Relat. Mater., 121 (2022) 108724. https://doi.org/10.1016/j.diamond.2021.108724
14. A.R. Ferdous, S.S. Shah, S.N.A. Shah, B.A. Johan, M.A. Al Bari, M.A. Aziz, Molecules, 29 (2024) 2081. https://doi.org/10.3390/molecules29092081
15. K. Sasaki, K. Yamamoto, M. Narahara, Y. Takabe, S. Chae, G. Panomsuwan, T. Ishizaki, Materials, 17 (2024) 320. https://doi.org/10.3390/ma17020320
16. G.B. Choi, Y.A. Kim, D. Hong, Y. Choi, S.H. Yeon, Y.K. Park, G.G. Lee, H. Lee, S.C. Jung, Carbon, 205 (2023) 444–453. https://doi.org/10.1016/j.carbon.2023.01.042
17. N. Saengarunthong, P. Khongthong, G. Panomsuwan, T. Ueno, N. Saito, A. Eiad-Ua, Key Eng. Mater., 751 (2017) 773–778. https://doi.org/10.4028/www.scientific.net/KEM.751.773
18. K. Fricke, H. Steffen, T. Von Woedtke, K. Schröder, K. Weltmann, Plasma Process. Polym., 8 (2011) 51–58. https://doi.org/10.1002/ppap.201000093
19. N. Britun, T. Minea, S. Konstantinidis, R. Snyders, J. Phys. Appl. Phys., 47 (2014) 224001. https://doi.org/10.1088/0022-3727/47/22/224001
20. S. Deng, N. Takeuchi, T. Kaneko, Materials, 18 (2025) 5662. https://doi.org/10.3390/ma18245662
21. M.K. Mun, W.O. Lee, J.W. Park, D.S. Kim, G.Y. Yeom, D.W. Kim, Appl. Sci. Converg. Technol., 26 (2017) 164–173. https://doi.org/10.5757/ASCT.2017.26.6.164
22. A.C. Ferrari, J. Robertson, Phys. Rev. B, 61 (2000) 14095. https://doi.org/10.1103/PhysRevB.61.14095
23. T. Qiu, J.G. Yang, X.J. Bai, Y.L. Wang, RSC Adv., 9 (2019) 12737–12746. https://doi.org/10.1039/C9RA00343F
24. L. Kong, Y. Zhu, P.J. Williams, M. Kabbani, F.R. Brushett, J.L.M. Rupp, J. Mater. Chem. A, 12 (2024) 4299–4311. https://doi.org/10.1039/D3TA07362A
25. K. Nikgoftar, A.K.M.R. Reddy, M.V. Reddy, K. Zaghib, Batteries, 11(4) (2025) 123. https://doi.org/10.3390/batteries11040123
26. D. Feng, X. Qin, L. Zheng, B. Guo, W. Dai, N. Song, L. Liu, Y. Xu, Z. Tang, T. Gao, Int. J. Electrochem. Sci., 19(3) (2024) 100488. https://doi.org/10.1016/j.ijoes.2024.100488
27. S. Li, W. Luo, Q. He, J. Lu, J. Du, Y. Tao, Y. Cheng, H. Wang, Int. J. Mol. Sci., 24(1) (2023) 284. https://doi.org/10.3390/ijms24010284
28. S. Villagómez-Salas, P. Manikandan, S.F.A. Guzmán, V.G. Pol, ACS Omega, 3(12) (2018) 17520–17527. https://doi.org/10.1021/acsomega.8b02290